

## Article

# Nanocrystalline Iron Oxides with Various Average Crystallite Size Investigated Using Magnetic Resonance Method

Rafał Pelka <sup>1</sup>, Urszula Nowosielecka <sup>1</sup>, Kamila Klimza <sup>1,\*</sup>, Izabela Moszyńska <sup>2</sup>, Konstantinos Aidinis <sup>3</sup>, Grzegorz Żołnierkiewicz <sup>4</sup>, Aleksander Guskos <sup>4</sup> and Nikos Guskos <sup>4</sup>

<sup>1</sup> Department of Inorganic Chemical Technology and Environment Engineering, Faculty of Chemical Technology and Engineering, West Pomeranian University of Technology in Szczecin, Szczecin, Piastów Ave. 42, 71-065 Szczecin, Poland

<sup>2</sup> Wałbrzych Municipal Waterworks and Sewage Systems Company, Al. Wyzwolenia Str., 58-300 Wałbrzych, Poland

<sup>3</sup> Department of Electrical and Computer Engineering, Ajman University, Ajman P.O. Box 346, United Arab Emirates

<sup>4</sup> Department of Applied Physics, West Pomeranian University of Technology, Szczecin, Al. Piastow 48, 70-311 Szczecin, Poland

\* Correspondence: kk50381@zut.edu.pl

**Abstract:** A series of nanocrystalline iron oxide samples (M1–M5) which differ from each other in average crystallite size (from 26 to 37 nm) was studied. The raw material was nanocrystalline iron with an average crystallite size equal to 21 nm promoted with hardly reducible oxides: Al<sub>2</sub>O<sub>3</sub>, CaO, K<sub>2</sub>O (in total, max. 10 wt%). Nanocrystalline iron was subjected to oxidation with water vapor to achieve different oxidation degrees ( $\alpha = 0.16$ –1.00). Metallic iron remaining in the samples after the oxidizing step was removed by etching. Magnetic resonance spectra of all samples were obtained at room temperature. All resonance lines were asymmetric and intense. These spectra were fitted by Lorentzian and Gaussian functions. All spectral parameters depend on the preparation method of the nanoparticles. We suppose that the Lorentz fit gives us a spectrum from larger agglomerated sizes whereas the Gaussian fit comes from much smaller magnetic centers. For the nanocrystalline samples with the largest size of iron oxide nanocrystallites, the highest value of total integrated intensity was obtained, indicating that at smaller sizes, they are more mobile in reorientation processes resulting in more settings of anti-parallel magnetic moments. The magnetic anisotropy should also increase with the increase in size of nanocrystallites.

**Keywords:** iron oxides; nanocrystallites; magnetic resonance; magnetic properties; nanocrystallite size distribution



**Citation:** Pelka, R.; Nowosielecka, U.; Klimza, K.; Moszyńska, I.; Aidinis, K.; Żołnierkiewicz, G.; Guskos, A.; Guskos, N. Nanocrystalline Iron Oxides with Various Average Crystallite Size Investigated Using Magnetic Resonance Method. *Crystals* **2024**, *14*, 363. <https://doi.org/10.3390/cryst14040363>

Academic Editor: Benilde F. O. Costa

Received: 6 March 2024

Revised: 4 April 2024

Accepted: 7 April 2024

Published: 11 April 2024



**Copyright:** © 2024 by the authors. Licensee MDPI, Basel, Switzerland. This article is an open access article distributed under the terms and conditions of the Creative Commons Attribution (CC BY) license (<https://creativecommons.org/licenses/by/4.0/>).

## 1. Introduction

Nanocrystalline iron oxides find applications in various fields. They are used as contrast agents in magnetic resonance imaging (MRI), enabling precise imaging of anatomical and pathological structures. Additionally, they are employed in theranostics, combining diagnostics with therapy, especially in cancer treatment, where they can act as drug carriers [1–6].

In the environmental protection sector, nanocrystalline iron oxides are utilized for removing contaminants from groundwater and wastewater [7–9], serving as adsorbents or catalysts in purification processes. Furthermore, in magnetic therapy, magnetic nanoparticles can be employed for targeted heating of areas containing these nanoparticles, which is being explored as a supportive method in cancer treatment. Nanocrystalline iron oxides are also used as drug carriers, facilitating the targeted delivery of drugs to specific cells or areas in organisms, and iron oxide nanoparticles obtained through environmentally friendly methods are also being investigated for their potential as effective antioxidants, anti-inflammatory agents, and treatments for diabetes [10,11].

Research on their magnetic properties can contribute not only to development in the field of medicine, but also in materials engineering. The application of nanocrystalline iron oxides in materials technology is promising and encompasses several areas. In the production of magnetic materials, they can be used to create advanced magnets, employed in electromachines and electronic devices. In electronics, iron oxide nanoparticles may find use in the production of advanced electronic components, potentially in data storage, microprocessors, and magnetic memory technology, but they can be used as material for energy storage as well [12–15]. Additionally, intensive research on new materials with unique properties focuses on nanocrystalline iron oxides, contributing to the development of superior construction materials, corrosion-resistant coatings, and materials with special properties like self-regeneration or high-temperature resistance. As a result, the application of iron oxides in materials technology has the potential to accelerate progress in the field of modern materials with diverse and advanced properties, influencing the development of various industries and technologies [16,17].

These diverse applications highlight the potential of nanocrystalline iron oxide particles in the fields of medicine, environmental protection, and technology. However, continued research is crucial for a comprehensive understanding of their safety and effectiveness in various contexts.

Magnetic oxide iron fine particles have traditionally attracted intense research interest, e.g., [18–27]. They exhibit a number of physical phenomena related to the so-called size effects. In addition to the interest in understanding the nature and mechanisms of such new phenomena, there is a technological drive due to the immediate applications of these systems, mainly in high-density magnetic recording media. Some of these outstanding phenomena accompanying the size reduction are related to the transition to a single-domain magnetic structure, for instance, low Curie temperature, high magnetic susceptibility, superparamagnetism, large coercivities, quantum tunneling of magnetization, giant magnetoresistance, etc. [6,18–23,28,29]. Therefore, nanoparticles—as submicron particles of which a single unit is sized from 1 to 100 nm and made of inorganic or organic materials—exhibit many novel properties compared with the bulk materials.

In particular, magnetite nanoparticles offer potential for clearer imaging of tissue and organs; furthermore, nano-magnetite can be modified to allow for organ-specific imaging. Scientists are now trying to develop mechanisms that allow drugs to go directly to a certain area of the human body. For instance, if someone has liver cancer and a drug has been developed to combat such a disease, the drug can be attached to magnetite nanoparticles through a series of methods, then the nano-magnetite can be delivered directly to the liver, and the drug can be released there.

Additionally, spintronics represents an important research area in solid-state devices due to its nature of spin-dependent carrier transport behavior [22,23]. In the work [30], strong magnetic interactions of nanocrystalline  $\alpha$ -Fe of different sizes of nanocrystallites were examined. The coexistence of a superparamagnetic state was shown and the parameters of magnetic resonance strongly depended on the dimensions of the nanocrystallites [30]. Therefore, there is a strong need to study the properties of nanoparticles of given sizes and not only the average values of some parameters measured for the whole set consisting of nanocrystallites of various sizes.

The works presented above lead to the conclusion that nanomaterials already have many applications and even more potential opportunities ahead. However, due to their specific structure (nanometric dimensions), it also turns out that physical and chemical properties of nanomaterials depend on the size of crystallites. It can even be said that when determining the chemical and physical properties of nanomaterials, the size of the nanoparticles is an additional state parameter (in addition to, e.g., the chemical and phase composition) that should be taken into account [31]. Therefore, determining individual properties for specific sizes of nanocrystallites (and not only the average values of the tested parameters for the entire set of nanocrystallites with a wide range of diameters) is particularly important. Therefore, methods were searched for to separate fractions of

nanomaterial containing specified crystallite sizes from a substance with a broad crystallite size distribution. For this purpose, based on the reaction model [32], a pioneering chemical method was developed [30,33] to allow the separation of proper crystallite fractions from nanocrystalline material comprising of crystallites with different sizes (raw nanomaterial with a wide range of nanocrystallite sizes). That chemical method was applied to prepare tested samples both in work [30] and for the current investigations. As a result, as a research material we have developed stable, sponge-like nanocomposites of metals or their oxides with specific nanocrystallite sizes (in practice, narrowed ranges of nanocrystallite size distributions).

In this work, we wanted to demonstrate the correct operation of this nanocrystallite selection method using a different (second) system—previously we tested the obtained nanocrystallites of metallic iron, and now it is nanocrystalline magnetite.

In the context of the presented application perspectives of nanomaterials, with particular emphasis on nanocrystalline iron oxides, the aim of the work is to prepare the series of nanocrystalline iron oxide samples (M1–M5) containing nanocrystallites of a particular size—to confirm the efficiency of the innovative chemical method [30] for another chemical system (iron oxides)—and study their magnetic properties using the magnetic resonance method in the context of the extremely important and prospective magnetic properties of such nanomaterials as a function of the size of their nanocrystallites. It is expected that in the current work, iron oxides will have much weaker magnetic interactions than iron; hence, the resonance lines are less shifted from  $g = 2$  [18] and are more mobile in the processes of reorientation of magnetic moments. Therefore, one of the most sensitive research methods for dynamic interactions, which is magnetic resonance, was used. On the other hand, the superparamagnetic state more visible even at room temperature may reveal itself more.

## 2. Experimental

The raw material used to prepare samples of nanocrystalline iron oxides was nanocrystalline iron doped with hardly reducible oxides— $\text{Al}_2\text{O}_3$ ,  $\text{CaO}$  and  $\text{K}_2\text{O}$ . These dopes were present in an amount of several percent by weight and provide thermal stability to iron nanocrystallites and develop their surface [30–34]. The nanocrystalline form of iron was obtained via two high-temperature processes—fusion and reduction. In the first step, magnetite (Sigma-Aldrich, Saint Louis, MO, USA) was fused with small amounts of  $\text{Al}_2\text{O}_3$  (Sigma-Aldrich, Saint Louis, MO, USA),  $\text{CaO}$  (Sigma-Aldrich, Saint Louis, MO, USA) and  $\text{KNO}_3$  (Chempur, Piekary Śląskie, Poland) at a temperature of  $1500\text{ }^\circ\text{C}$  according to the procedure described in detail in [35]. Then, the alloy was cooled down, crushed and sieved to select grains of the size  $1.0\text{--}1.2\text{ mm}$ . In the next step, this fraction of material was reduced polythermally to a temperature of  $500\text{ }^\circ\text{C}$ , with hydrogen (Air Liquide, Paris, France), under atmospheric pressure. Under such conditions, the iron oxide was reduced to metallic iron (nanocrystallite size distribution standard deviation  $\sigma = 15\text{ nm}$ ) and the promoter oxides mentioned above formed the bridges between iron nanocrystallites, preventing their sintering. After reduction, doped nanocrystalline iron was cooled down in a nitrogen (Air Liquide, Paris, France) atmosphere and passivated in order to avoid auto-ignition. This resulted in a sample of nanocrystalline iron, referred to as starting material, to prepare samples M1–M5.

Sample M1 was completely oxidized using only water vapor (oxidation degree  $\alpha = 1.00$ ). Samples of nanocrystalline iron oxides M2–M5 were obtained via a two-step procedure, of which the first stage consisted of high-temperature reactions of nanocrystalline iron with a gas phase and the second stage included reaction of the nanocrystalline iron in a liquid medium at room temperature (RT). The method was based on a patent [33] but expanded upon in accordance with a publication [30]. High-temperature processes were conducted in a tubular differential reactor with thermogravimetric measurement and a system for measuring the gas phase composition (designed and manufactured using our own resources and then certified by external authorities). An amount of  $1\text{ g}$  of passivated starting material was placed in a platinum basket in the form of single layer of grains

inside a reactor. The sample was heated in a temperature range from RT to 500 °C under a stream of hydrogen ( $12 \text{ dm}^3 \text{ H}_2/(\text{h g})$ ), which resulted in a reduction into a thin passive layer covering each iron nanocrystallite. After mass stabilizing, the gas atmosphere in the reactor was changed from reducing into inert through cut-off hydrogen flow and admitting nitrogen. In the next step, water vapor was introduced into the nitrogen stream (ca. 0.02 bar  $\text{H}_2\text{O}$ ; nitrogen flow  $12 \text{ dm}^3/(\text{h g})$ ) in order to conduct partial oxidation of the samples. Oxidation was carried out until the intended oxidation degrees in particular samples were achieved ( $\alpha = 0.16$  for M2,  $\alpha = 0.25$  for M3,  $\alpha = 0.33$  for M4 and  $\alpha = 0.45$  for M5). The oxidation degree was determined during the course of the process on the basis of the sample weight gain. After reaching the proper gain (which took around 1500 s for sample M2 up to 6000 s for sample M5), the atmosphere in the reactor was once more changed into inert, the temperature was decreased to RT and the partially oxidized sample was again passivated before its removal from the reactor. That way, the samples consisting of two phases—metallic unreacted iron and iron oxide (magnetite)—were obtained. The phase composition of iron and iron oxide as well as confirmation of the intended oxidation degrees were derived using the X-ray diffraction (XRD) method.

The second stage of preparation consisted of leaving only iron oxide phase in the samples by removing non-oxidized metallic iron via etching with diluted nitric acid (V) (Chempur, Piekary Śląskie, Poland). In order to increase the contact surface between the sample in the solid state with an etching agent, grains of the size 1.0–1.2 mm were triturated in an agate mortar. Powder samples were placed in a glass beaker with a capacity of 250 mL containing 100 mL of deionized water. Then, the diluted nitric acid with a concentration of  $3.64 \text{ mol/dm}^3$  was added dropwise from a burette. The amount of etching agent used was calculated based on an equation for the reaction of iron with nitric acid ( $\text{Fe} + 2\text{HNO}_{3,\text{diluted}} \rightarrow \text{Fe}(\text{NO}_3)_2 + \text{H}_2\uparrow$ ) and 10% excess was added. The content of the beaker was stirred continuously with a glass rod during acid dropping and after that, with a shaker for 24 h. The sample was subsequently rinsed several times with deionized water, filtered under reduced pressure and dried in a vacuum oven at a temperature of 70 °C for 12 h. The resulting samples M1–M5 were characterized using the XRD method—phase composition, nanocrystallite size distributions (NSD) and average size of nanocrystallites were determined.

The preparation procedure to obtain samples with a narrow nanocrystallite size distribution is illustrated in Figure 1.

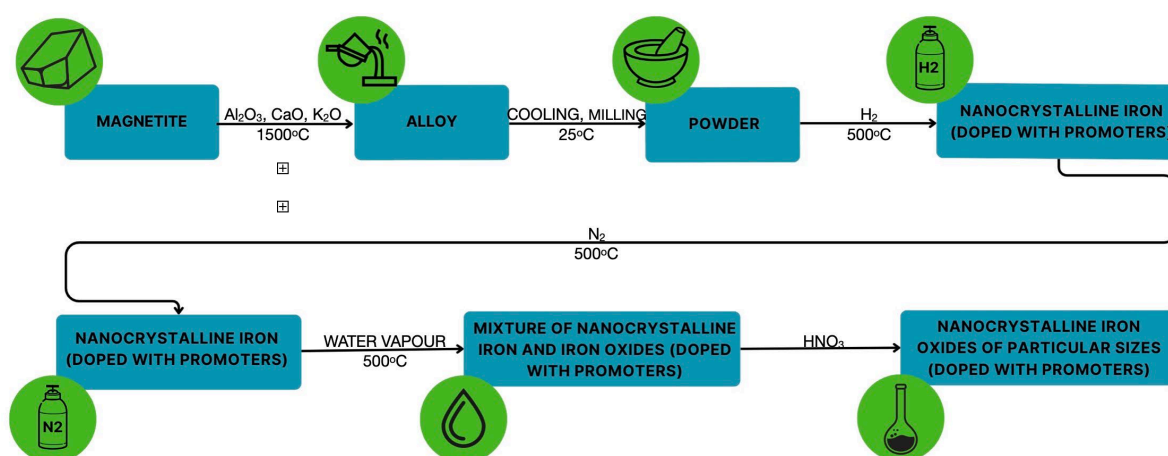


**Figure 1.** Scheme of the preparation procedure to obtain samples with narrow nanocrystallite size distribution.

XRD measurement for all samples in the M1–M5 series was performed using an X-ray diffractometer X’Pert Empyrean Philips (Malvern Panalytical Ltd, Malvern, UK). The source of the radiation was a copper lamp ( $k = 0.1540 \text{ nm}$ , accelerating voltage 35 kV, current 30 mA). An angle in the range  $10\text{--}110^\circ [2\theta]$ , with a step of  $0.05^\circ$  and count equal

to 400 s per step were applied. Phase analysis of the samples was carried out by means of the Rietveld method on the entire powder pattern. Calculations were performed using Philips X'Pert HighScore 3.0 software, based on crystallographic data contained in the identification card database ICDD PDF-4+. For the phase analysis, the cards of indices: 04-003-3884 (iron) and 04-007-1060 (magnetite) were used.

The method developed by Pielaszek was used to determine the nanocrystallite size distribution (NSD) [36,37]. This method uses advanced mathematical apparatus, thanks to which, by analyzing the geometry of a specific diffraction reflection, the shape of the size distribution of nanocrystallites of a given phase is calculated.

The measurements of magnetic resonance spectra of nanocrystallites M1–M5 were performed on a conventional X band ( $\nu = 9.4$  GHz) Bruker E 500 spectrometer (Bruker, Billerica, MA, USA) with 100 kHz magnetic field modulation. Nanocrystallites containing around 0.02 g powder were placed in 0.004 m-diameter quartz tubes. The magnetic field was scaled with an NMR magnetometer. The measurements were taken at room temperature. For all EPR spectra, the typical spectroscopic parameters were determined: g-spectroscopic splitting factor value, peak-to-peak line width ( $\Delta H$ ) and integral intensity with an accuracy of 0.1%.

Specific surface areas were measured using the volumetric method (using the Brunauer–Emmet–Teller (BET) equation and automated apparatus AutoChem II 2920, Micromeritics, Norcross, GA, USA).

To investigate the morphological properties of the obtained iron oxide samples, transmission electron microscopy (TEM, Tecnai F30 with a field emission gun operating at 200 kV, Thermo Fisher Scientific, Waltham, MA, USA) was applied.

### 3. Results and Discussion

Under the experimental conditions (high-temperature stage), a phase transformation occurs as a result of the oxidation reaction between nanocrystalline iron and water vapor. Oxygen atoms become integrated into the  $\alpha$ -iron crystal lattice and once the critical concentration of oxygen in iron is surpassed, a transition to the magnetite crystal lattice occurs throughout the entire volume of individual nanocrystallites [32]. In these (kinetic) conditions, the crystals undergo transformation from the smallest to the largest, whereas under conditions close to equilibrium, this order is reversed [31,38–40].

After the oxidation process, non-oxidized iron was removed from the samples by etching with dilute nitric acid (V). This resulted in a series of samples with a composition close to 100% magnetite and different mean crystallite sizes and standard deviations of NSD (Table 1), which was determined on the basis of measurements using the XRD method (magnetite nanocrystals' lattice parameter determined for studied samples: M1 0.8350 nm, M2 0.8362 nm, M3 0.8377 nm, M4 0.8390 nm and M5 0.8385 nm; these values are slightly lower than the value for stoichiometric magnetite, which is 0.8396 nm)—an example diffractogram for sample M4 is shown in Figure 2 (for the remaining samples, the results obtained were practically indistinguishable and similar to these)—and Pielaszek's method. The average nanocrystallite size of iron oxide/magnetite is a function of the degree of oxidation.

**Table 1.** Composition of samples after etching.

Sample Name	Fe <sub>3</sub> O <sub>4</sub>			Fe		FeO	
	Average Size	Standard Deviation of NSD	Phase Content	Average Size	Phase Content	Average Size	Phase Content
	nm	nm	%	Nm	%	nm	%
M1	26	15.0	93.7	15	6.0	na	0.3
M2	29	2.5	94.0	24	6.0	-	-
M3	32	5.0	95.0	19	5.0	-	-

Table 1. Cont.

Sample Name	Fe <sub>3</sub> O <sub>4</sub>			Fe		FeO	
	Average Size	Standard Deviation of NSD	Phase Content	Average Size	Phase Content	Average Size	Phase Content
	nm	nm	%	Nm	%	nm	%
M4	35	7.0	99.3	Na	0.4	na	0.3
M5	37	10.0	98.8	Na	1.2	-	-

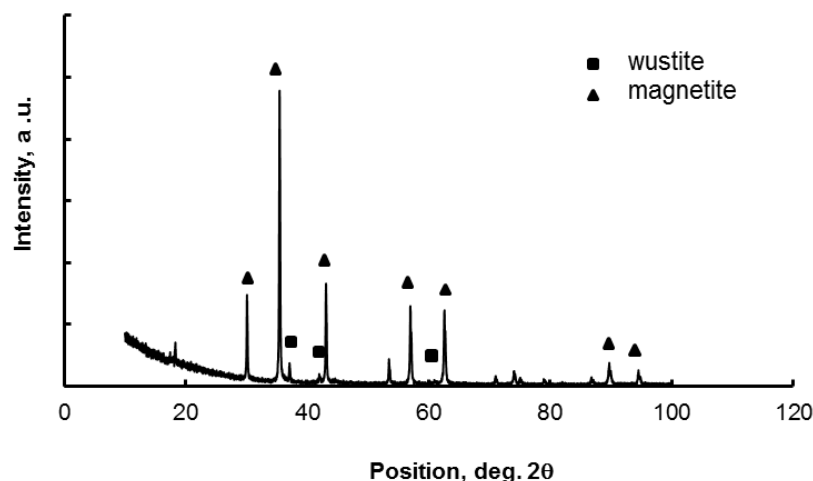
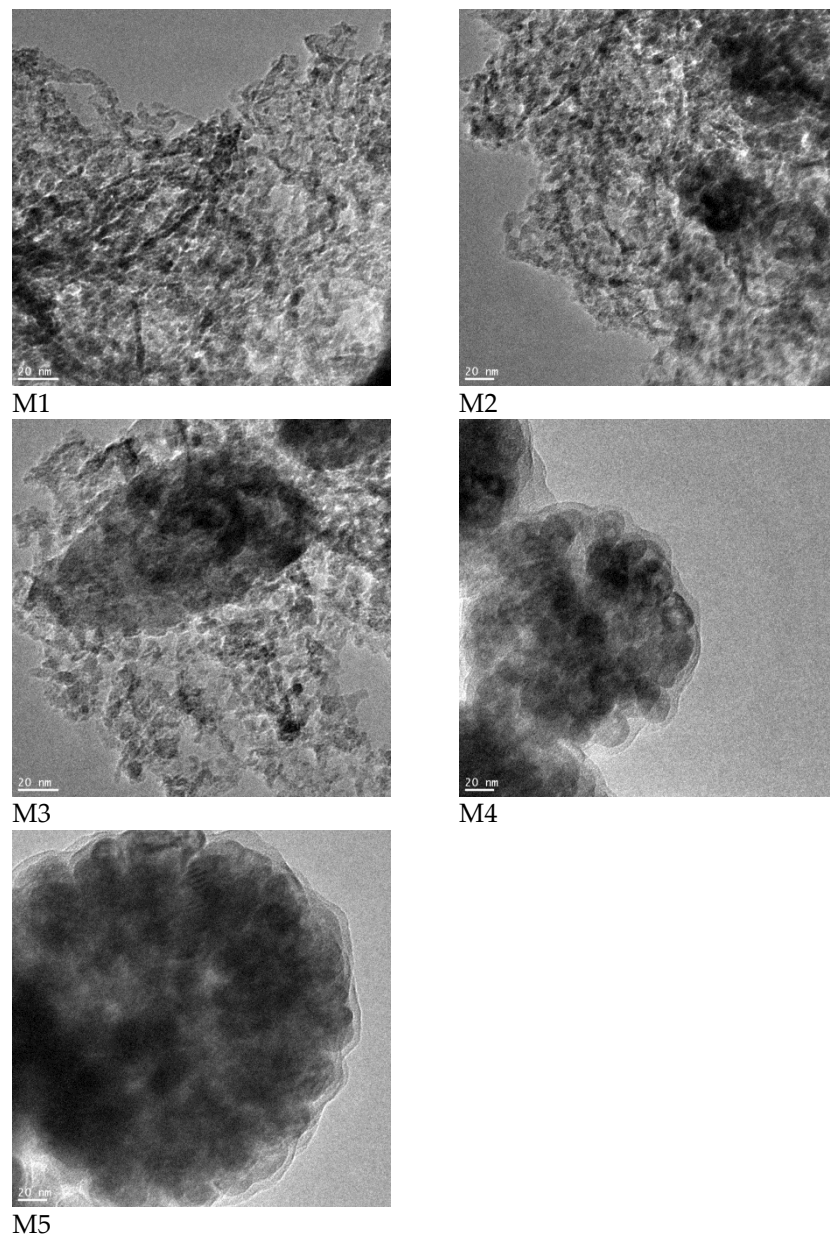


Figure 2. Diffractogram of sample M4 after the oxidation and etching stage with nitric acid (V).

The tested nanomaterial is actually a kind of sponge-like nanocomposite (visible to the naked eye, the grains may be of micrometer or millimeter size). It consists of nanocrystallites of the main phase (magnetite in the currently tested samples) separated from each other so effectively that chemically, they can certainly be treated as individual elements of the system [31,38–40]. They are separated from each other by a matrix—a layer of promoters (Al<sub>2</sub>O<sub>3</sub>, CaO, K<sub>2</sub>O—their total amount does not exceed 10% by mass) forming surface structures and glass phase bridges between individual nanocrystallites (ultimately, the samples are porous—the porosity coefficient is 0.5). Therefore, the values regarding the size of nanocrystallites presented in Table 1 refer to these individual, separated elements of the ‘nanocomposite’ system.

In the mentioned paper [31], it was stated that in a state close to equilibrium, nanocrystallites undergo a transformation from the largest to the smallest and average size of nanocrystallites decreased for every tested sample. This has been confirmed using the CPPR method, described in numerous studies [41,42]. However, the range of change in the average nanocrystallite size is narrower in the case of modified samples (like M2–M5; the change was 5 nm) as compared to the reference sample (like M1; the change was 37 nm). This clearly confirmed that nanocrystallite size distributions for samples M2–M5 were narrower than those for sample M1 (Table 1) and the efficiency of the method for the separation of nanocrystallites was evidenced as well. TEM microscopic images taken from different perspectives and their digital statistical analysis are consistent with the results obtained by XRD and Pielaszek’s method. Selected relevant TEM images are shown in Figure 3.

The specific surface areas were examined and it turned out the values were similar to those presented elsewhere [30]. It was found that the modified samples showed a 1.6–2.5-times increase in specific surface area compared to the reference sample M1 (Table 2).



**Figure 3.** TEM images of samples M1–M5 after the oxidation and etching stage with nitric acid (V).

**Table 2.** Analysis results for specific surface area of samples M1, M2, M3, M4 and M5 (BET equation).

Sample Name	Specific Surface Area [m <sup>2</sup> /g]
M1	8.77
M2	13.75
M3	22.30
M4	16.60
M5	17.10

Magnetic resonance spectra have been investigated and are presented in Figure 4. For all samples, they have intense resonance signal characteristics for iron oxide [18]. For the starting material, the magnetic resonance spectra were characteristic of iron [43]. This indicates strong magnetic interacting materials. The recorded magnetic resonance spectra were similar to the ones for Fe<sub>3</sub>O<sub>4</sub> and were fitted with the sum of two lines: one Gaussian-

shaped and one Lorentzian-shaped for each sample and a very good fit was received (Figure 5). All magnetic resonance parameters depended on the amount of magnetic agglomerates as well as the crystallite sizes. Resonance lines from Fe were not analyzed because they had very low intensity.

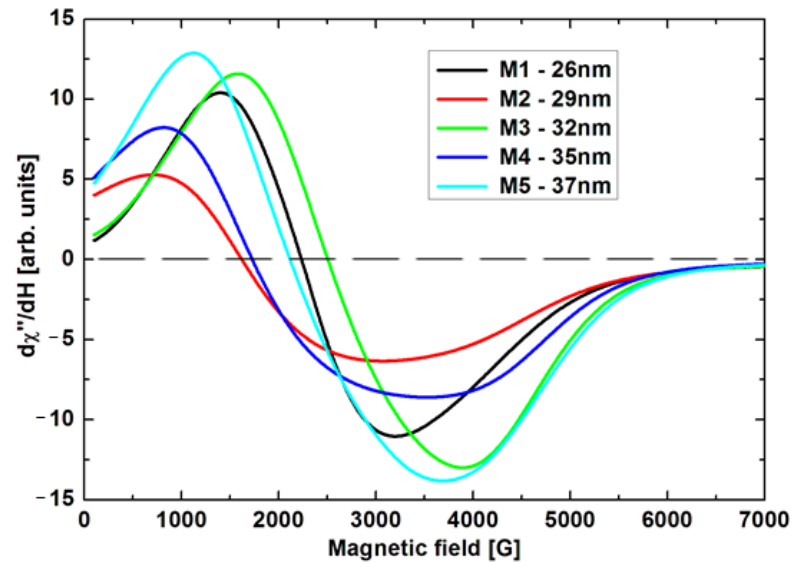


Figure 4. The FMR spectra of nanocrystalline samples at room temperature.

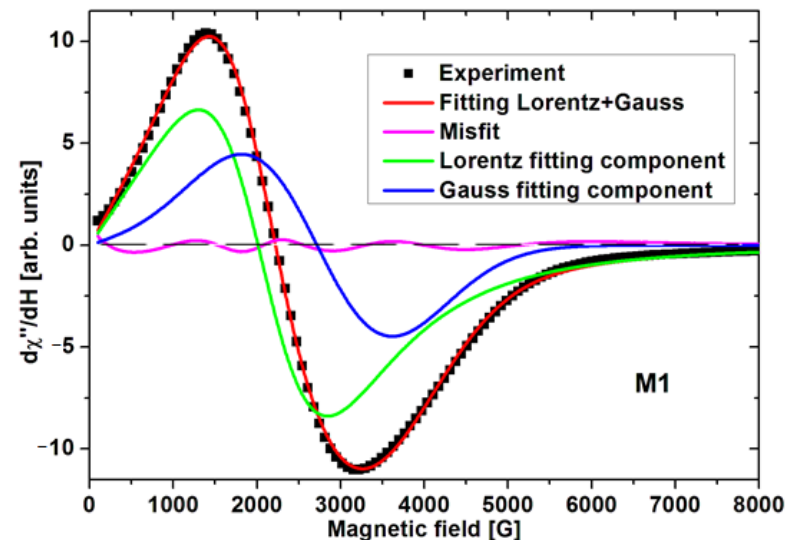


Figure 5. Experimental and fitting spectra, Gauss and Lorentz curves, as well as the misfit curve for nanocomposite M1 at room temperature.

Figure 5 presents experimental and fitting magnetic resonance spectra as well as Gauss and Lorentz curves, and the misfit curve for the nanocomposite M1. Very good fits were also obtained for all other samples.

In Table 3, the parameters of the FMR spectra are given, taken from Figures 6–10. Fluctuations in the positions of the lines depending on the sample are noticeable. They are associated with the reorientation processes of nanoparticles (creating an internal field that superimposes on the external field). The linewidths indicate dipole interactions. An increasing trend in the difference of magnetic fields is noticeable for samples M1–M4. Integrated intensity carries information about magnetic moments associated with nanoparticles (Lorentzian and Gaussian fitting). The integrated Gaussian intensity is assigned to smaller nanoparticle sizes. An increasing trend is noticeable for samples M1–M5. Hence, upon

summation, we obtained the total intensity and a growing trend is visible (last column). This may signify potential applications in targeted anticancer therapy. After introducing appropriately prepared nanoparticles into cancer tissue, each of their excitations by an external magnetic field will result in heat generation and the destruction of cancer cells without harming healthy cells.

**Table 3.** Parameters of the FMR spectra taken from Figures 6–10 for samples: M1, M2, M3, M4 and M5.

Sample	Size [nm]	Resonance Field [G]		Difference of Resonance Field $H_0G-H_0L$ [G]	Linewidth [G]		Integrated Intensity $I_{int}$ [arb. units]		Total Integrated Intensity $I_{int}$ [arb. Units]
		Lorentz	Gauss		Lorentz	Gauss	Lorentz	Gauss	
M1	26	2058	2718	660	1601	1801	5.07	3.62	8.70
M2	29	1324	2356	1032	1568	2499	2.87	6.78	9.65
M3	32	2144	3209	1065	1578	1680	6.07	5.38	1.44
M4	35	1341	2458	1117	1522	2523	3.67	10.75	14.42
M5	37	1539	2606	1067	1649	2344	4.46	15.08	19.54

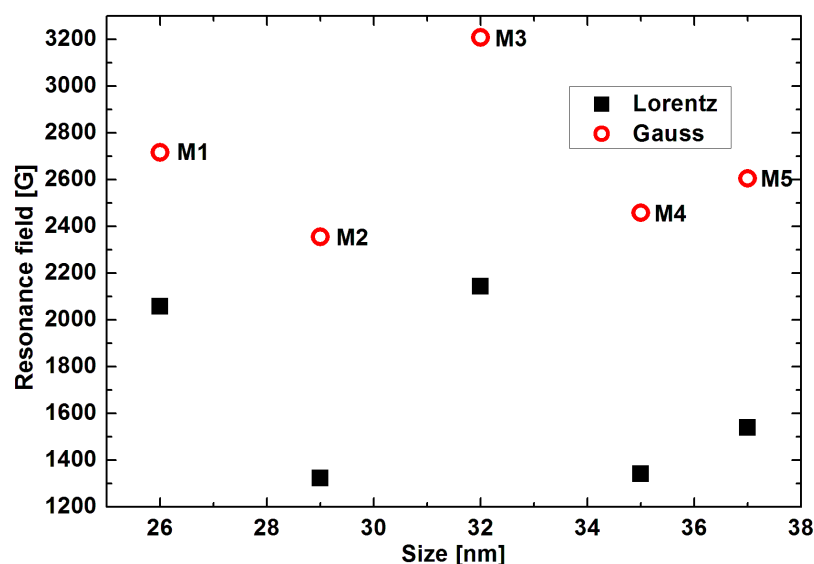


**Figure 6.** The position of resonance lines.

In Figure 6, the dependencies of the position of resonance lines on the sizes of nanocrystallites are given. The reorientation processes of the collective spin system affected the internal magnetic field and changed the resonance condition ( $h\nu = g\mu_B (H_0 - H_{int})$ ), where  $h$ —Planck constant,  $\nu$ —resonance frequency,  $\mu_B$ —Bohr magneton,  $H_0$ —the applied external magnetic field and  $H_{int}$ —the internal magnetic field). For resonance line fitting by Gaussian function, the internal magnetic field was essentially greater than the resonance line fitted by Lorentzian function. The greatest shift towards the lower fields of the Lorentz resonance line was seen in the M2 sample, but resonance lines for the M3 sample were the least shifted (Figure 6). The positions of the resonance lines are much smaller up to the distance  $g = 2$  than in nanocrystalline  $\alpha$ -Fe [32]. Hence, the stronger the interactions between nanocrystallites, the greater the shift caused by creating larger internal magnetic fields.

Figure 7 presents the differences in the position of resonance lines depending on the content of  $Fe_3O_4$  in the samples. The smallest differences were observed for the M1 sample and then we have a sharp increase. As the content of magnetite increases, we have an increase in this and the greatest value was achieved for the M4 sample. The presence of two resonance lines may indicate a magnetic anisotropy. So, the greatest magnetic anisotropy can be expected for larger-sized nanocrystallites. This is due to lower mobility in reorientation processes.

Figure 8 shows the linewidth of the investigated nanocrystalline samples. A very broad linewidth was obtained for all samples. Lower linewidths and some changes in linewidth were observed for resonance lines fitted using the Lorentzian function. The linewidths of the nanocrystalline samples resonance lines fitted using Gaussian functions were greater. For samples with a nanocrystalline size of 35 nm, the differences were the greatest (over 1000 G). This very large linewidth could be due to the inhomogeneous broadening arising from the distribution of the easy-axis direction in nanoparticles [44]. It could be produced by a distribution of resonance field, which could be experimentally represented as an inhomogeneous broadening of magnetic resonance linewidth.

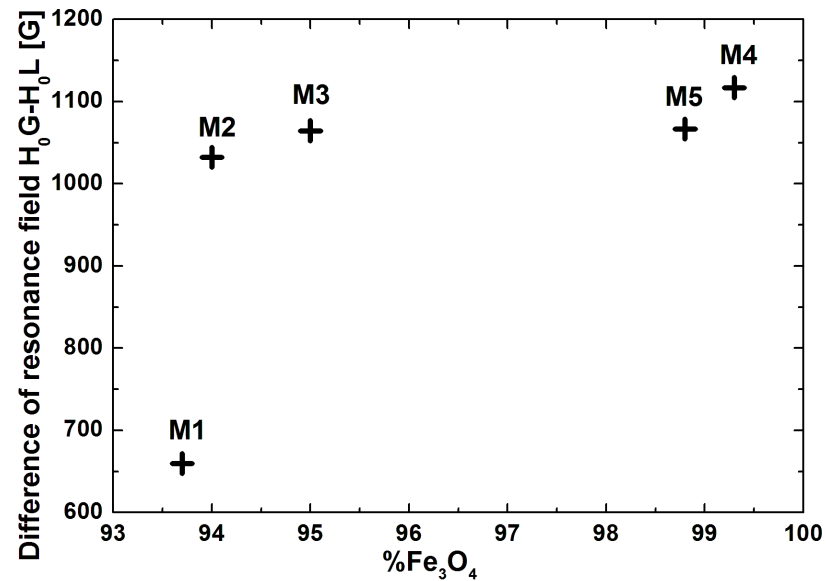


Figure 7. The difference in position of the resonance lines obtained by fitting the Lorentz and Gaussian functions.

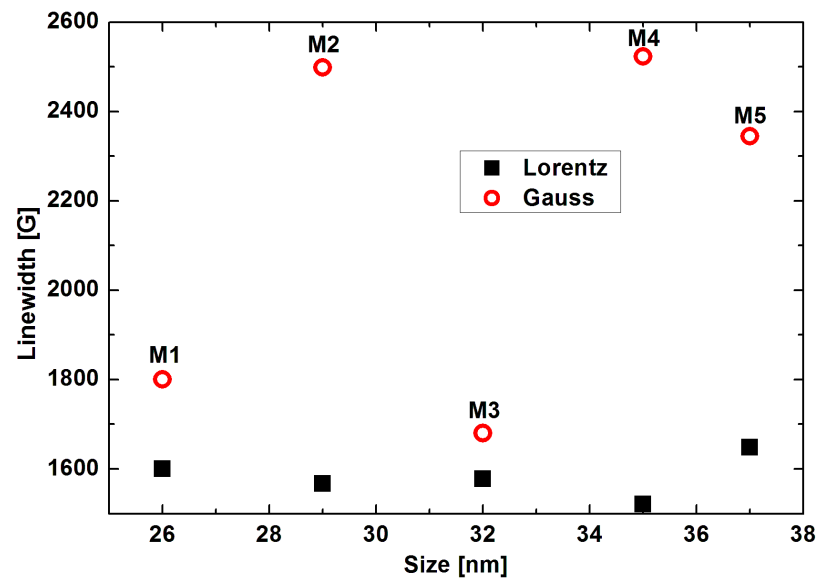


Figure 8. The linewidths of the investigated nanocrystalline samples as a function of nanocrystallite sizes.

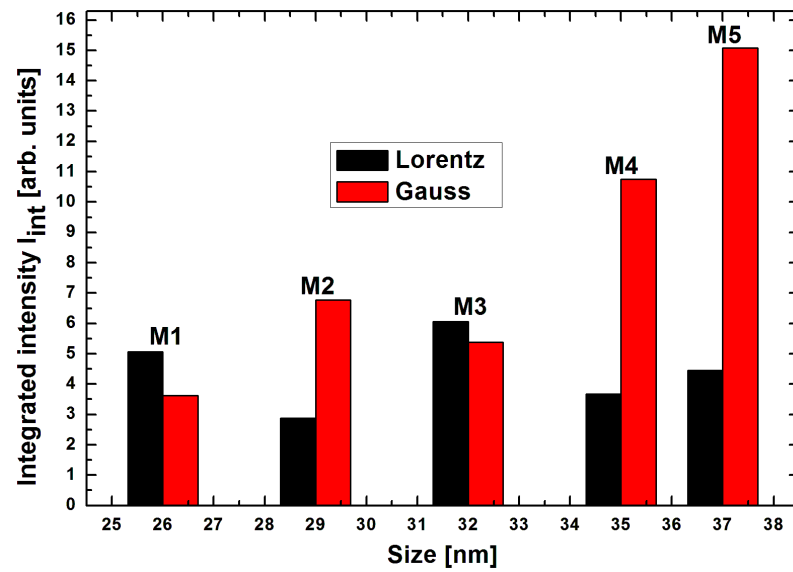


Figure 9. The dependence of intensities on the size of nanocrystallites.

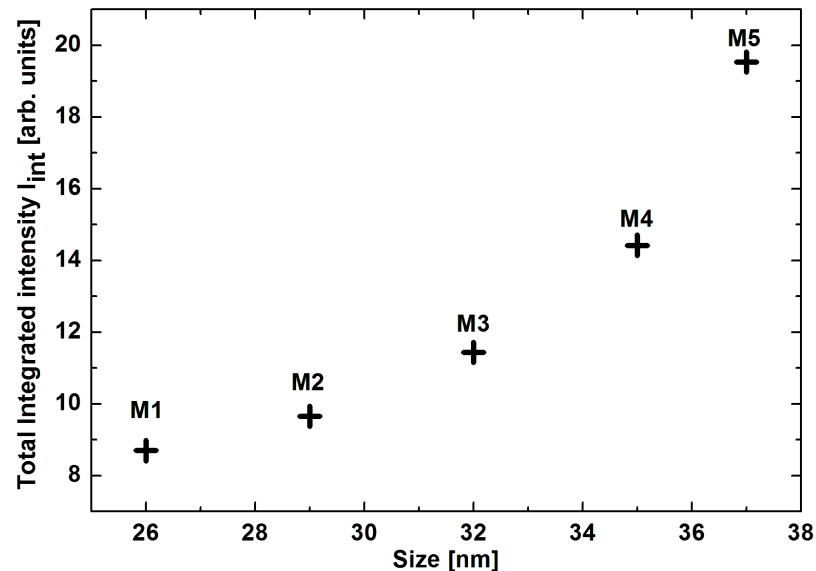


Figure 10. The dependence of total integrated intensity on the size of nanocrystallites.

The intensity was calculated from the relationship  $I = A\Delta H^2$  where  $I$ —intensity,  $A$ —amplitude and  $\Delta H$ —linewidth. Figure 9 shows the dependence of the intensity on the size of the nanocrystallites of the resonance line matched by Gaussian (red) and Lorentzian function (black). The resonance line matched by Gaussian function significantly dominates the M2, M4 and M5 samples. It is likely that we had two systems of correlated spins of different sizes where the latter were much smaller in size. They can be located at existing pores in nanocrystalline samples. It could also be a measure of the number of pores in the samples. This explains why there were resonance lines closer to  $g = 2$ , as well as why they have a larger linewidth of resonance lines (Figures 6 and 8). This might also explain why the largest difference in position of the resonance lines was obtained for sample M4.

Figure 10 shows the dependence of total integrated intensity on the size of nanocrystallites. With an increase in size of nanocrystallites, intensities increased and the largest increase was obtained for the M5 nanoparticles. The integrated intensity had a similar character with an increasing concentration of iron nanoparticles as in the process where the influence of carburization levels by methane decomposition on nanocrystalline iron was investigated [44].

This can be explained assuming that smaller-sized nanocrystallites are more mobile in reorientation processes. In our case, it means that many magnetic moments can line up parallel to each other with smaller crystallite sizes in a superparamagnetic state.

The results of the current work and those published previously (in particular [30,38]) prove that nanocrystallites can be segregated using the developed chemical method and thermally stabilized with structure-forming promoters. It was also confirmed using another example of a reaction system that the physical properties of nanocrystallites are a function not only of their chemical and phase composition, but also of their size.

#### 4. Conclusions

A series of nanocrystalline iron oxides which differ from each other in average crystallite size (from 26 to 37 nm) was prepared. All parameters describing the magnetic resonance strongly depend on the size of the nanocrystallites of the studied nanoparticles. Magnetic resonance measurements showed the presence of two systems of correlated spins of different sizes. The increase in the total integrated intensity with the increase in the size of the nanocrystallites is due to the process of reorientation of the magnetic moments. The smaller nanocrystallites are more mobile and can more easily reach a superparamagnetic state, setting the magnetic moments anti-parallel. Because we have magnetic moments of different magnitude that can arrange themselves in an anti-parallel way, a “ferrimagnetic” state can arise. This has a significant impact on magnetic susceptibility as well as on magnetic anisotropy. The smaller the size of the nanocrystallites, the more likely the reorientation mobility of magnetic moments. Hence, at smaller sizes, nanocrystallites take a more active role in anti-parallel ordering.

It is worth emphasizing that both the applied research technique and the research direction itself are characterized by an innovative approach. The obtained results, combined with previously published results (in particular in [30,38]), confirmed that nanocrystallites can be segregated using the developed chemical method and thermally stabilized with structure-forming promoters. It was also verified using another example of a reaction system that the physical properties of nanocrystallites are a function not only of their chemical and phase composition, but also of their size.

**Author Contributions:** Conceptualization, R.P. and N.G.; methodology, K.A., N.G. and R.P. validation, U.N., I.M. and G.Ž.; formal analysis, R.P. and A.G.; investigation, U.N., I.M., G.Ž. and A.G.; data curation, R.P. and N.G.; writing—original draft preparation, I.M., N.G., K.A. and R.P.; writing—review and editing, N.G., R.P., K.K., I.M. and U.N.; visualization, G.Ž., K.K. and A.G.; supervision, R.P. and N.G.; project administration, R.P.; funding acquisition, R.P. All authors have read and agreed to the published version of the manuscript.

**Funding:** This research was funded by The National Science Centre, Poland, grant number 2017/27/B/ST8/02970.

**Data Availability Statement:** Data are contained within the article.

**Conflicts of Interest:** Author Aleksander Guskos was employed by the company Contec. The remaining authors declare that the research was conducted in the absence of any commercial or financial relationships that could be construed as a potential conflict of interest.

#### References

1. Urbanova, V.; Magro, M.; Gedanken, A.; Baratella, D.; Vianello, F.; Zboril, R. Nanocrystalline Iron Oxides, Composites, and Related Materials as a Platform for Electrochemical, Magnetic, and Chemical Biosensors. *Chem. Mater.* **2014**, *26*, 6653–6673. [[CrossRef](#)]
2. Armijo, L.M.; Brandt, Y.I.; Mathew, D.; Yadav, S.; Maestas, S.; Rivera, A.C.; Cook, N.C.; Withers, N.J.; Smolyakov, G.A.; Adolphi, N.L.; et al. Iron Oxide Nanocrystals for Magnetic Hyperthermia Applications. *Nanomaterials* **2012**, *2*, 134–146. [[CrossRef](#)] [[PubMed](#)]
3. Clemons, T.D.; Viola, H.M.; House, M.J.; Hool, L.C.; Iyer, K.S. *Nanomaterials: Science and Applications*; Kane, D.M., Micolich, A., Roger, P., Eds.; Jenny Stanford Publishing: Boca Raton, FL, USA, 2016; pp. 23–30.
4. Sabu, V.; Shirin, V.K.A.; Sankar, R.; Pramod, K. *Nanomaterials and Nanotechnology in Medicine*; Visakh, P.M., Ed.; Wiley: Hoboken, NJ, USA, 2022; p. 385.

5. Mahmoudi, M.; Sant, S.; Wang, B.; Laurent, S.; Sen, T. Superparamagnetic iron oxide nanoparticles (SPIONs): Development, surface modification and applications in chemotherapy. *Adv. Drug Deliv. Rev.* **2011**, *63*, 24–46. [[CrossRef](#)] [[PubMed](#)]
6. Pal, S.; Dutta, P.; Shah, N.; Huffman, G.; Seehra, M. Surface Spin Disorder in Fe<sub>3</sub>O<sub>4</sub> Nanoparticles Probed by Electron Magnetic Resonance Spectroscopy and Magnetometry. *IEEE Trans. Magn.* **2007**, *43*, 3091–3093. [[CrossRef](#)]
7. Buzukashvili, S.; Hu, W.; Sommerville, R.; Brooks, O.; Kökkılıç, O.; Rowson, N.A.; Ouzilleau, P.; Waters, K.E. Magnetic Zeolite: Synthesis and Copper Adsorption Followed by Magnetic Separation from Treated Water. *Crystals* **2023**, *13*, 1369. [[CrossRef](#)]
8. Xu, P.; Zeng, G.; Huang, D.; Feng, C.; Hu, S.; Zhao, M.; Lai, C.; Wei, Z.; Huang, C.; Xie, G.; et al. Use of iron oxide nanomaterials in wastewater treatment: A review. *Sci. Total Environ.* **2012**, *424*, 1–10. [[CrossRef](#)] [[PubMed](#)]
9. Rahman, A.; Daniel, L.S.; Uahengo, V. Iron Oxide Nanomaterials for Water Purification. In *Novel Materials and Water Purification: Towards a Sustainable Future*; Kyriakopoulos, G.L., Zamparas, M.G., Eds.; Royal Society of Chemistry: London, UK, 2024; pp. 234–255. [[CrossRef](#)]
10. Abuzeid, H.M.; Julien, C.M.; Zhu, L.; Hashem, A.M. Green Synthesis of Nanoparticles and Their Energy Storage, Environmental, and Biomedical Applications. *Crystals* **2023**, *13*, 1576. [[CrossRef](#)]
11. Meng, Y.Q.; Shi, Y.N.; Zhu, Y.P.; Liu, Y.Q.; Gu, L.W.; Liu, D.D.; Ma, A.; Xia, F.; Guo, Q.Y.; Xu, C.C.; et al. Recent trends in preparation and biomedical applications of iron oxide nanoparticles. *J. Nanobiotechnol* **2024**, *22*, 24. [[CrossRef](#)] [[PubMed](#)]
12. Kalidass, J.; Anandan, S.; Sivasankar, T. Sonoelectrochemical Nanoarchitectonics of Crystalline Mesoporous Magnetite @ Manganese Oxide Nanocomposite as an Alternate Anode Material for Energy-Storage Applications. *Crystals* **2023**, *13*, 557. [[CrossRef](#)]
13. Wirecka, R.; Marzec, M.M.; Marciszko-Wiąckowska, M.; Lis, M.; Gajewska, M.; Trynkiewicz, E.; Lachowicz, D.; Bernasik, A. The effect of shell modification in iron oxide nanoparticles on electrical conductivity in polythiophene-based nanocomposites. *J. Mater. Chem. C* **2021**, *9*, 10453–10461. [[CrossRef](#)]
14. Imran, M.; Chaudhary, A.A.; Ahmed, S.; Alam, M.M.; Khan, A.; Zouli, N.; Hakami, J.; Rudayni, H.A.; Khan, S.-U.-D. Iron Oxide Nanoparticle-Based Ferro-Nanofluids for Advanced Technological Applications. *Molecules* **2022**, *27*, 7931. [[CrossRef](#)] [[PubMed](#)]
15. Malasi, A.; Taz, H.; Farah, A.; Patel, M.; Lawrie, B.; Pooser, R.; Baddorf, A.; Duscher, G.; Kalyanaraman, R. Novel Iron-based ternary amorphous oxide semiconductor with very high transparency, electronic conductivity and mobility. *Sci. Rep.* **2015**, *5*, 18157. [[CrossRef](#)] [[PubMed](#)]
16. Gleiter, H. Nanostructured materials: Basic concepts and microstructure. *Acta Mater.* **2000**, *48*, 1–29. [[CrossRef](#)]
17. Kushwaha, A.K.; John, M.; Misra, M.; Menezes, P.L. Nanocrystalline Materials: Synthesis, Characterization, Properties, and Applications. *Crystals* **2021**, *11*, 1317. [[CrossRef](#)]
18. Guskos, N.; Anagnostakis, E.A.; Likodimos, V.; Typek, J.; Maryniak, M.; Narkiewicz, U. Ferromagnetic resonance and ac conductivity of a polymer composite of Fe<sub>3</sub>O<sub>4</sub> and Fe<sub>3</sub>C nanoparticles dispersed in a graphite matrix. *J. Appl. Phys.* **2005**, *97*, 024304. [[CrossRef](#)]
19. Ghosh, R.; Pradhan, L.; Devi, Y.P.; Meena, S.S.; Tewari, R.; Kumar, A.; Sharma, S. Induction heating studies of Fe<sub>3</sub>O<sub>4</sub> magnetic nanoparticles capped with oleic acid and polyethylene glycol for hyperthermia. *J. Mater. Chem.* **2011**, *21*, 13388–13398. [[CrossRef](#)]
20. Teymourian, H.; Salimi, A.; Khezrian, S. Fe<sub>3</sub>O<sub>4</sub> magnetic nanoparticles/reduced graphene oxide nanosheets as a novel electrochemical and bioelectrochemical sensing platform. *Biosens. Bioelectron.* **2013**, *49*, 1–8. [[CrossRef](#)]
21. Venkateswarlu, S.; Rao, Y.S.; Balaji, T.; Prathima, B.; Jyothi, N.V.V. Biogenic synthesis of Fe<sub>3</sub>O<sub>4</sub> magnetic nanoparticles using plantain peel extract. *Mater. Lett.* **2013**, *100*, 241–244. [[CrossRef](#)]
22. Ding, Y.; Shen, S.Z.; Sun, H.; Sun, K.; Liu, F.; Qi, Y.; Yan, J. Design and construction of polymerized-chitosan coated Fe<sub>3</sub>O<sub>4</sub> magnetic nanoparticles and its application for hydrophobic drug delivery. *Mater. Sci. Eng. C Mater. Biol. Appl.* **2015**, *48*, 487–498. [[CrossRef](#)] [[PubMed](#)]
23. Prasad, C.; Yuvaraja, G.; Venkateswarlu, P. Biogenic synthesis of Fe<sub>3</sub>O<sub>4</sub> magnetic nanoparticles using Pisum sativum peels extract and its effect on magnetic and Methyl orange dye degradation studies. *J. Magn. Magn. Mater.* **2017**, *424*, 376–381. [[CrossRef](#)]
24. Ma, Y.; Xu, G.; Wei, F.; Cen, Y.; Xu, X.; Shi, M.; Cheng, X.; Chai, Y.; Sohail, M.; Hu, Q. One-Pot Synthesis of a Magnetic, Ratiometric Fluorescent Nanoprobe by Encapsulating Fe<sub>3</sub>O<sub>4</sub> Magnetic Nanoparticles and Dual-Emissive Rhodamine B Modified Carbon Dots in Metal-Organic Framework for Enhanced HClO Sensing. *ACS Appl. Mater. Interfaces* **2018**, *10*, 20801–20805. [[CrossRef](#)] [[PubMed](#)]
25. Sajjadi, A.; Mohammadi, R. Fe<sub>3</sub>O<sub>4</sub> magnetic nanoparticles (Fe<sub>3</sub>O<sub>4</sub> MNPs): A magnetically reusable catalyst for synthesis of Benzimidazole compounds. *J. Med. Chem. Sci.* **2019**, *2*, 55–58. [[CrossRef](#)]
26. Guo, W.; Fu, Z.; Zhang, Z.; Wang, H.; Liu, S.; Feng, W.; Zhao, X.; Giesy, J.P. Synthesis of Fe<sub>3</sub>O<sub>4</sub> magnetic nanoparticles coated with cationic surfactants and their applications in Sb(V) removal from water. *Sci. Total Environ.* **2020**, *710*, 136302. [[CrossRef](#)] [[PubMed](#)]
27. Marć, M.; Najder-Kozdrowska, L.; Guskos, N.; Żołnierkiewicz, G.; Montero, A.M.; Dudek, M.R. The Use of Ultra-Small Fe<sub>3</sub>O<sub>4</sub> Magnetic Nanoparticles for Hydrothermal Synthesis of Fe<sup>3+</sup>-Doped Titanate Nanotubes. *Materials* **2020**, *13*, 4612. [[CrossRef](#)] [[PubMed](#)]
28. Patsula, V.; Moskvina, M.; Dutz, S.; Horak, D. Size-dependent magnetic properties of iron oxide nanoparticles. *J. Phys. Chem. Solids* **2016**, *88*, 24–30. [[CrossRef](#)]
29. Chen, L.; Xie, J.; Wu, H.; Li, J.; Wang, Z.; Song, L.; Zang, F.; Ma, M.; Gu, N.; Zhang, Y.; et al. Precise Study on Size-Dependent Properties of Magnetic Iron Oxide Nanoparticles for In Vivo Magnetic Resonance Imaging. *J. Nanomater.* **2018**, *2018*, 3743164. [[CrossRef](#)]

30. Nowosielecka, U.; Pelka, R.; Moszyńska, I.; Guskos, N.; Typek, J.; Żolnierkiewicz, G. Studies of magnetic properties of nanocrystalline iron of different sizes of nanocrystallites. *J. Magn. Magn. Mater.* **2017**, *443*, 324–333. [[CrossRef](#)]
31. Arabczyk, W.; Ekiert, E.; Pelka, R. Size-dependent transformation of  $\alpha$ -Fe into  $\gamma'$ -Fe<sub>4</sub>N in nanocrystalline the Fe-NH<sub>3</sub>-H<sub>2</sub> system. *J. Phys. Chem. C* **2016**, *120*, 17989–17995. [[CrossRef](#)]
32. Wróbel, R.; Arabczyk, W. Solid–Gas Reaction with Adsorption as the Rate Limiting Step. *J. Phys. Chem. A* **2006**, *110*, 9219. [[CrossRef](#)] [[PubMed](#)]
33. Arabczyk, W.; Lendzion-Bieluń, Z.; Wróbel, R. Sposób Otrzymywania Nanomateriałów na Bazie Żelaza i Kobaltu o Określonych Rozmiarach Krystalitów. Polish Patent No. P206909, 21 May 2010.
34. Lubkowski, K.; Arabczyk, W.; Grzmil, B.; Michalkiewicz, B.; Pattek-Janczyk, A. Passivation and oxidation of an ammonia iron catalyst. *Appl. Catal. A-Gen.* **2007**, *329*, 137–147. [[CrossRef](#)]
35. Arabczyk, W.; Ziebro, J.; Kałucki, K.; Świerkowski, R.; Jakrzewska, M. Instalacja laboratoryjna do ciągłego wytopu katalizatorów żelazowych. *Chemik* **1996**, *1*, 22.
36. Pielaszek, R. FW15/45M method for determination of the grain size distribution from powder diffraction line profile. *J. Alloys Compd.* **2004**, *382*, 128–132. [[CrossRef](#)]
37. Pielaszek, R. Analytical expression for diffraction line profile for polydispersive powders. In *Applied Crystallography, Proceedings of the XIX Conference, Kraków, Poland, 1–4 September 2003*; World Scientific Publishing: Singapore, 2004; pp. 43–50. [[CrossRef](#)]
38. Wilk, B.; Arabczyk, W. Investigation of nitriding and reduction processes in the nanocrystalline iron-ammonia-hydrogen system at 350°C. *Phys. Chem. Chem. Phys.* **2015**, *17*, 20185–20193. [[CrossRef](#)]
39. Moszyński, D.; Kiełbasa, K.; Arabczyk, W. Influence of crystallites' size on iron nitriding and reduction of iron nitrides in nanocrystalline Fe–N system. *Mater. Chem. Phys.* **2013**, *141*, 674–679. [[CrossRef](#)]
40. Moszyński, D. Nitriding of Nanocrystalline Iron in the Atmospheres with Variable Nitriding Potential. *J. Phys. Chem. C* **2014**, *118*, 15440–15447. [[CrossRef](#)]
41. Wilk, B.; Błachowski, A.; Lendzion-Bieluń, Z.; Arabczyk, W. Thermodynamics of Chemical Processes in the System of Nanocrystalline Iron–Ammonia–Hydrogen at 350 °C. *Catalysts* **2020**, *10*, 1242. [[CrossRef](#)]
42. Wilk, B.; Pelka, R.; Arabczyk, W. Study of the Iron Catalyst for Ammonia Synthesis by Chemical Potential Programmed Reaction Method. *Phys. Chem. C* **2017**, *121*, 8548–8556. [[CrossRef](#)]
43. Maryniak, M.; Guskos, N.; Typek, J.; Kucharewicz, I.; Narkiewicz, U.; Roslaniec, Z.; Kwiatkowska, M.; Arabczyk, W.; Aidinis, K. FMR study of polymer composites with nanocrystalline iron-carbon fillers. *Rev. Adv. Mater. Sci.* **2006**, *12*, 200–205.
44. Helminiak, A.; Arabczyk, W.; Żolnierkiewicz, G.; Guskos, N.; Typek, J. FMR study of the influence of carburization levels by methane decomposition on nanocrystalline iron. *Rev. Adv. Mat. Sci.* **2011**, *29*, 166–174.

**Disclaimer/Publisher's Note:** The statements, opinions and data contained in all publications are solely those of the individual author(s) and contributor(s) and not of MDPI and/or the editor(s). MDPI and/or the editor(s) disclaim responsibility for any injury to people or property resulting from any ideas, methods, instructions or products referred to in the content.